optica

Condition for perfect antireflection by optical resonance at material interface

KEN XINGZE WANG,[1] ZONGFU YU,[1,2] SUNIL SANDHU,[1] VICTOR LIU,[1,3] AND SHANHUI FAN[1,*]

[1]Ginzton Lab, Stanford University, Stanford, California 94305, USA

[2]Currently at: Department of Electrical and Computer Engineering, University of Wisconsin-Madison, Madison, Wisconsin 53706, USA

[3]Currently at: Palo Alto Research Center (PARC), 3333 Coyote Hill Road, Palo Alto, California 94304, USA

*Corresponding author: shanhui@stanford.edu

Reflection occurs at an air–material interface. The development of antireflection schemes, which aims to cancel such reflection, is important for a wide variety of applications including solar cells and photodetectors. Recently, it has been demonstrated that a periodic array of resonant subwavelength objects placed at an air–material interface can significantly reduce reflection that otherwise would have occurred at such an interface. Here, we introduce the theoretical condition for complete reflection cancellation in this resonant antireflection scheme. Using both general theoretical arguments and analytical temporal coupled-mode theory formalisms, we show that in order to achieve perfect resonant antireflection, the periodicity of the array needs to be smaller than the free-space wavelength of the incident light for normal incidence, and also the resonances in the subwavelength objects need to radiate into air and the dielectric material in a balanced fashion. Our theory is validated using first-principles full-field electromagnetic simulations of structures operating in the infrared wavelength ranges. For solar cell or photodetector applications, resonant antireflection has the potential for providing a low-cost technique for antireflection that does not require nanofabrication into the absorber materials, which may introduce detrimental effects such as additional surface recombination. Our work here provides theoretical guidance for the practical design of such resonant antireflection schemes.   © 2014 Optical Society of America

1. INTRODUCTION

Reflection occurs at the interface between air and a dielectric. In many applications, for example, solar cells and photodetectors, such a reflection is detrimental to system performance and thus an effective antireflection strategy is required. A standard approach includes single- or multi-layer interference [1–6], and adiabatic optical impedance matching [7–16], frequently at the nanoscale [17–23].

In recent years, a new approach for antireflection has been proposed and widely adopted [24–33]. In this approach, one places arrays of nanoparticles at or near the air–dielectric interface (Fig. 1). These particles support Mie resonances [34,35]. The antireflection effect is associated with the excitation of the

Mie resonances. This approach has several unique potential beneficial characteristics compared to other approaches [36–40]. First, unlike the tapering geometry (for the adiabatic impedance matching) that is commonly done by etching into the active material, which may increase surface recombination, the resonant antireflection can be achieved by simply coating the surface with nanoparticles without an etching process [24,28,41]. Second, the optical resonances might in addition provide light trapping functionalities [28,41–47], might enhance the broadband antireflection performance indirectly, for example, by influencing the material dispersion [48], and might allow tunability of the spectral range of antireflection [49].
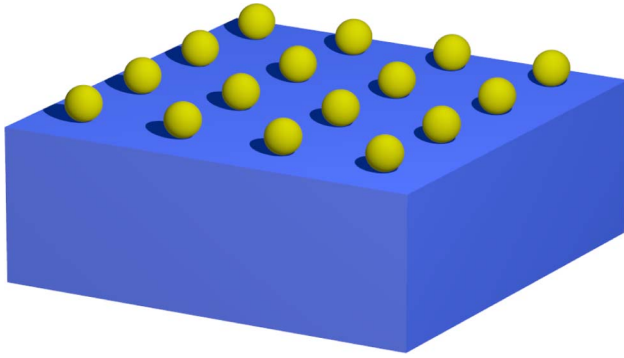
Fig. 1. Nanostructure array at an air–dielectric interface for resonant antireflection. The blue region represents a dielectric whose refractive index is greater than that of air. The yellow regions represent subwavelength structures that support optical resonances. Here, for concreteness, we draw a square lattice; other lattices can be used as well. The lattice constant or periodicity is a in all dimensions. Light is incident from top, and the wavelength is λ.

The experimental demonstration in Refs. [24–27] raised important theoretical questions regarding the conditions for complete antireflection from resonance. In Ref. [24], the antireflection effect is attributed to the tendency of the resonance to radiate dominantly into the dielectric. In this paper, we present a theoretical analysis for complete antireflection. Contrary to the claim in Ref. [24], here we show theoretically that complete antireflection is possible only if the resonance radiates to both the air side and the dielectric side in a balanced manner. In addition, the periodicity of the structure needs to be smaller than the free-space wavelength for normally incident light. We validate the theoretical results with numerical simulations.

2. THEORY

We first provide a set of general arguments to support the main conclusions of this paper, using the concepts that underly Fano interference in optical resonator systems [50]. In the absence of resonance, there is reflection and transmission at the air–dielectric interface. Such a reflection and transmission process consists of part of what we will refer to as the "direct pathway." When resonant particles are placed at the interface, the reflection and transmission processes can be modified in two ways. First, there is in addition a "resonant pathway" for light transport, through which the incident light first excites the resonance; the energy in the resonance then decays, thus also contributing to the transmission or reflection amplitude. Second, away from the resonances, the presence of the particles would also contribute to the direct pathway since these particles, even when away from resonance, would provide physical perturbation to the air–dielectric interface. To achieve resonant antireflection, we would like the contributions to the reflection amplitude from the direct and resonant pathways to cancel each other. This immediately leads to two general considerations:

First, the resonance needs to radiate in a balanced fashion to the air and the dielectric sides. The result can be argued from reciprocity. If the resonances were to radiate completely into the dielectric substrate, it follows immediately by reciprocity that any incident light from the air side could not excite the resonance. And hence in such a case the resonance cannot play any role in the antireflection process. For the resonance to play a significant role in the antireflection process, the resonance needs to be excited significantly for light incident from the air side, which in turn requires significant radiation of the resonance to the air side.

Second, the periodicity of the array needs to be chosen such that there is only zeroth-order diffraction on the air side. For normally incident light from air, then, the periodicity of the array needs to be smaller than the free-space wavelength:

$$a < \lambda. \tag{1}$$

With Eq. (1) satisfied, complete antireflection would then be achieved if the direct and resonant reflections destructively interfere at the normal direction. On the other hand, if the periodicity of the array is greater than the free-space wavelength, there is more than one diffraction channel in the air, and in general it would be far more difficult to achieve complete cancellation on each of these channels.

Building upon the general arguments above, we now provide a theoretical description of the resonant antireflection process. Since the structure is periodic, we consider only a single unit cell containing a single resonant nanostructure as in Fig. 2. For simplicity, we consider only normally incident light
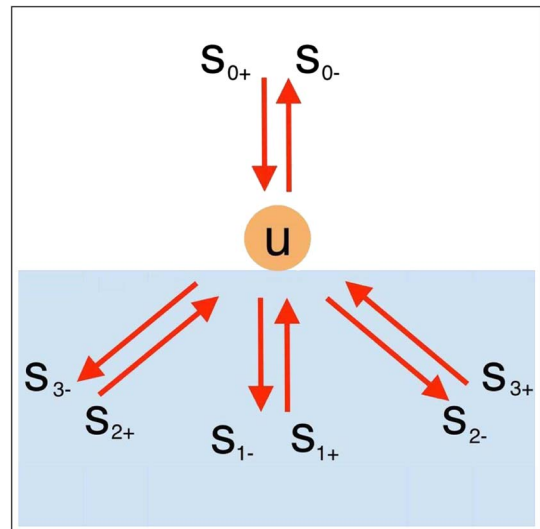

Fig. 2. Resonance and channels in a unit cell of Fig. 1. The resonant amplitude is denoted as u. At each channel, there are incoming and outgoing electromagnetic waves, as indicated by the red arrows. The incoming/outgoing wave amplitude at channel i is denoted as $s_{i\pm}$. For $i > 1$, the channel indices are chosen such that, in the absence of resonant scattering, incoming light at channel i undergoes total internal reflection to outgoing light at the same channel i if Eq. (1) is satisfied. For example, the input/output port of channel 2 is in the opposite direction to the output/input port of channel 3 (as opposed to the typical choice of the input and output ports of the same channel being in opposite directions, which we adopt for channels 0 and 1), and, as a result, the input/output light at channel i reflects at the interface to be the output/input light at the channel with the same index i since it cannot be directly coupled to the only channel in air (channel 0) or any other channels in the dielectric.

from the air side. We therefore apply the periodic boundary condition at the edge of the cell. We further assume that Eq. (1) is satisfied, and Fig. 2 reflects this property of the nano-structure array. Let $u \in \mathbb{C}$ be the complex amplitude of the resonance, and be so normalized that $|u|^2$ corresponds to the electromagnetic energy stored in the resonance. The inputs and outputs at the diffraction channels can be collectively written as column vectors of complex wave amplitudes:

$$\mathbf{s}_+ = \begin{pmatrix} s_{0+} \\ s_{1+} \\ s_{2+} \\ s_{3+} \\ \vdots \\ s_{N+} \end{pmatrix}, \qquad \mathbf{s}_- = \begin{pmatrix} s_{0-} \\ s_{1-} \\ s_{2-} \\ s_{3-} \\ \vdots \\ s_{N-} \end{pmatrix}, \qquad (2)$$

where the indices label different channels. Channel 0 is the zeroth-order diffraction channel in air, and as we argued above the only diffraction channel on the air side. All other channels are on the dielectric side, with channel 1 corresponding to the zeroth diffraction order. $N = 2\lfloor na/\lambda \rfloor + 1$ represents the total number of diffraction channels on the dielectric side, where n is the refractive index of the lossless dielectric and $\lfloor \cdot \rfloor$ is the floor function.

We describe the structure using the temporal coupled-mode theory [51–53]. The dynamics of the resonance are given by

$$\frac{du}{dt} = \left(j\omega_0 - \frac{1}{\tau} \right) u + \mathbf{d}^T \mathbf{s}_+, \qquad (3)$$

where j is the imaginary unit, $\omega_0 \in \mathbb{R}$ is the resonant frequency, $\tau \in \mathbb{R}$ is the total lifetime due to the decay of the resonance to all channels, $\mathbf{d} \in \mathbb{C}^{N+1}$ is the column vector of coupling constants between the resonance and the channels, and the superscript T stands for the matrix transpose. On the other hand, light transport among the channels passes through both the direct and the resonant pathways:

$$\mathbf{s}_- = C\mathbf{s}_+ + \mathbf{d}u, \qquad (4)$$

where $C \in \mathbb{C}^{(N+1)\times(N+1)}$ represents the scattering matrix for the direct pathway. By energy conservation and reciprocity, one can show that [50,52]

$$\mathbf{d}^\dagger \mathbf{d} = \frac{2}{\tau}, \qquad (5)$$

$$C\mathbf{d}^* = -\mathbf{d}. \qquad (6)$$

Next, we construct an explicit expression for the direct scattering matrix C. We assume that the direct process only involves channels 0 and 1 that correspond to normal propagating light on the air and the dielectric sides, respectively. We note that light at all other channels, which by construction are higher-order diffraction channels on the dielectric side, undergoes total internal reflection at the air–dielectric interface as Eq. (1) is satisfied [53]. By choosing appropriate reference planes for the incoming and outgoing waves, without loss of generality, the direct scattering matrix C can be written as

$$C = e^{j\phi} \begin{pmatrix} r & jt & 0 & 0 & \dots & 0 \\ jt & r & 0 & 0 & \dots & 0 \\ 0 & 0 & 1 & 0 & \dots & 0 \\ 0 & 0 & 0 & 1 & \dots & 0 \\ \vdots & \vdots & \vdots & \vdots & \ddots & \vdots \\ 0 & 0 & 0 & 0 & \dots & 1 \end{pmatrix}, \qquad (7)$$

where $r, t, \phi \in \mathbb{R}$ satisfies $r^2 + t^2 = 1$. r and t are the amplitude reflection and transmission coefficients, respectively, between channels 0 and 1, and is the phase factor determined by the choice of the reference planes [50,54].

We define the overall scattering matrix $S \in \mathbb{C}^{(N+1)\times(N+1)}$ as follows:

$$\mathbf{s}_- \equiv S\mathbf{s}_+. \qquad (8)$$

The complex amplitude reflection coefficient for the normally incident light in Fig. 1 is given by the first diagonal element in S as defined by Eq. (8). Using Eqs. (3), (4), and (7), with a harmonic input of frequency ω, the power reflection coefficient can then be written as

$$R = \left| re^{j\phi} + \frac{d_0^2}{j(\omega - \omega_0) + \frac{1}{\tau}} \right|^2, \qquad (9)$$

where d_0, the first element of $\mathbf{d}$, is the coupling constant of the resonance to channel 0 in Fig. 2. One could express d_0 in terms of r, ϕ, and the decay lifetimes using Eqs. (5)–(7):

$$d_0^2 = \frac{-e^{j\phi}\left(\frac{2}{\tau_0}\right)^2}{r\left(\frac{1}{\tau_0} + \frac{1}{\tau_1}\right) + \frac{1}{r}\left(\frac{1}{\tau_0} - \frac{1}{\tau_1}\right) \mp j\sqrt{2\left(\frac{1}{\tau_0^2} + \frac{1}{\tau_1^2}\right) - r^2\left(\frac{1}{\tau_0} + \frac{1}{\tau_1}\right)^2 - \frac{1}{r^2}\left(\frac{1}{\tau_0} - \frac{1}{\tau_1}\right)^2}}. \qquad (10)$$

Substituting Eq. (10) into Eq. (9), we obtain

$$R = \frac{\left[r(\omega - \omega_0) \mp \sqrt{2\left(\frac{1}{\tau_0^2} + \frac{1}{\tau_1^2}\right) - r^2\left(\frac{1}{\tau_0} + \frac{1}{\tau_1}\right)^2 - \frac{1}{r^2}\left(\frac{1}{\tau_0} - \frac{1}{\tau_1}\right)^2} \right]^2 + \left[r\sum_{i=2}^{N} \frac{1}{\tau_i} - \frac{1}{r}\left(\frac{1}{\tau_0} - \frac{1}{\tau_1}\right) \right]^2}{(\omega - \omega_0)^2 + \left(\frac{1}{\tau}\right)^2}. \qquad (11)$$

In Eqs. ([10](#)) and ([11](#)), $\tau_i = 2/|d_i|^2$ is the contribution to the decay lifetime of the resonance from leakage to channel i for any $i = 0, \ldots, N$, and $1/\tau = \sum_{i=0}^{N} 1/\tau_i$. Equation ([11](#)) implies that complete antireflection, i.e., $R = 0$, can only be achieved if

$$\frac{1}{\tau_0} = \frac{1}{\tau_1} + r^2 \sum_{i=2}^{N} \frac{1}{\tau_i}. \tag{12}$$

Then, complete antireflection occurs at the frequency

$$\omega = \omega_0 \mp \sqrt{\frac{2}{r^2}\left(\frac{1}{\tau_0^2} + \frac{1}{\tau_1^2}\right) - \left(\frac{1}{\tau_0} + \frac{1}{\tau_1}\right)^2 - \frac{1}{r^4}\left(\frac{1}{\tau_0} - \frac{1}{\tau_1}\right)^2}. \tag{13}$$

Although the decay rates need to exactly satisfy Eq. ([12](#)) for complete antireflection, the deviation from 100% transmission depends quadratically on the difference between the two sides of Eq. ([12](#)). For example, a 5% increase in τ_0 would roughly result in a 1% reduction from perfect transmission when the resonant antireflection scheme is used for an air–silicon interface.

Equations ([1](#)) and ([12](#)) together represent a sufficient condition in order to achieve perfect resonant antireflection. It is interesting to note that, if the periodicity is smaller than the wavelength *in the dielectric*, i.e., there is only one channel in the dielectric, Eq. ([12](#)) implies that complete antireflection is only achievable when the resonance decays *equally* to the air and the dielectric sides, in consistency with the conclusion in Ref. [54].

3. SIMULATION

In the following, we validate these theoretical results. The procedure of our numerical validation is to first construct a system that indeed exhibits complete resonant antireflection, and then show that, for such a system, its numerically simulated spectrum is well explained by Eq. ([11](#)). For this purpose and for simplicity without loss of generality, we therefore simulate structures with geometries shown in Fig. [1](#) with a one-dimensional instead of a full two-dimensional array, using rigorous coupled wave analysis (RCWA) [55]. We vary the parameters of the structures until complete resonant antireflection is achieved. For such a structure that exhibits complete resonant antireflection, we then check its numerically obtained reflection spectrum against Eq. ([11](#)). In Eq. ([11](#)), both the resonant frequency ω_0 and various decay rates τ_i are extracted from finite-difference time-domain (FDTD) simulations of the same structure where we excite the resonance and then study its decay in the time domain [56]. The direct reflection coefficient r can be determined by stripping off the resonant features and then fitting the background of the simulated spectrum [57]. Since the conditions for complete resonant antireflection, i.e., Eq. ([12](#)), are a direct exact consequence of Eq. ([11](#)), a numerical validation of Eq. ([11](#)) therefore confirms our main theoretical results about the conditions of complete resonant antireflection.
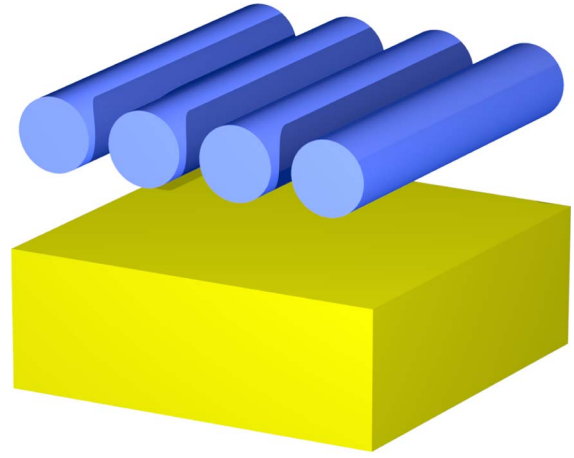

Fig. 3. High-Q resonant antireflection structure consisting of an array of infinitely long cylindrical rods above an air–dielectric interface. The blue regions represent a silicon-like lossless dielectric with a dielectric constant of 12. The yellow region represents a silicon-nitride-like lossless dielectric with a refractive index of 2, which is assumed to be infinitely thick in the lower half space. The periodicity of the nanorod array is 1 μm. The radius of each rod is 390 nm. The distance between the bottom of the silicon rods and the air–silicon-nitride interface is 430 nm.

We first consider a hypothetical structure in Fig. [3](#), where a periodic array of infinitely long cylindrical rods with a radius of 390 nm and a periodicity of 1 μm is placed at a distance of 430 nm from an air–substrate interface. The nanorods are made of a silicon-like lossless material with a dielectric constant of 12, and the substrate is made of a silicon-nitride-like lossless material with a refractive index of 2. Such a structure supports high-Q resonances because the separation weakens the resonant decay in the silicon into the silicon-nitride substrate, which is assumed to be infinitely thick in the lower half space. In practice, a spacer layer is required to mechanically support the silicon rods, and, if a low-refractive-index dielectric such as silicon dioxide were chosen as the spacer material, the physics would be similar to this hypothetical scenario.

In Fig. [4(a)](#), we show the simulated transmission spectrum (red curve) of the structure in Fig. [3](#). Without the nanostructure, the direct transmission coefficient would be $T = 1 - r^2 = 1 - [(n - 1)/(n + 1)]^2 = 0.8889$ (green dash-dot line). We plot the steady state electric field intensity in the absence of the nanostructure at $\lambda = 1300$ nm in Fig. [4(c)](#). The interference pattern in air indicates significant reflection at this interface. With the nanorods, there exist a low-Q resonance ($Q \sim 10^0$) at around $\lambda = 1236$ nm [Fig. [4(d)](#)] with a nearly unity power transmission $T = 0.9985$, and two high-Q resonances ($Q \sim 10^2$) at around $\lambda = 1265$ nm [Fig. [4(e)](#)] and $\lambda = 1371$ nm [Fig. [4(f)](#)], with nearly unity power transmission $T = 0.9975$ and $T = 0.9959$, respectively. Each of the resonances decays to three channels in the dielectric below, and the far-field intensity in air is nearly uniform because most reflection is eliminated. The resonances therefore indeed provide near-complete antireflection. Using the procedures outlined in the previous paragraph, we calculate the theory curve (blue dashed curve) using Eq. ([11](#)) in the vicinity of each resonance. In Fig. [4(a)](#), the direct transmission is taken
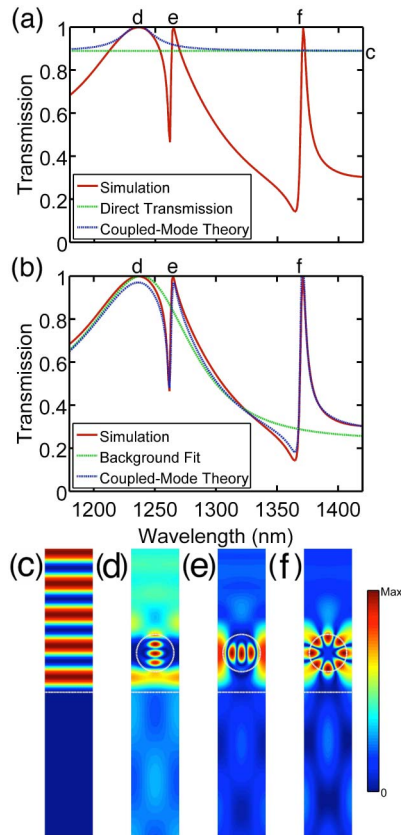
Fig. 4. Transmission spectrum and steady state electric field intensity plots for the structure in Fig. 3 at normal incidence. (a),(b) Comparison of transmission spectra by theory and by simulation. The theory data (blue dashed curves) are computed using Eq. (11) with decay rates obtained from FDTD simulations. The simulation data (red curves) are obtained from a RCWA simulation. (a) The direct transmission (green dash-dot line) is determined analytically as $T = 1 - r^2 = 1 - [(n-1)/(n+1)]^2 = 0.8889$, which serves as the background process in Eq. (11). (b) The background process is determined using a fit to the low-Q resonance spectrum. The red simulation curve is identical to that in Fig. 1. (c)–(f) Electric field intensity plots. The dashed white curves are material boundaries. The colorbar is relative and log-scaled, and red and blue colors correspond to high and low intensities, respectively. (c) Steady state electric field intensity at $\lambda = 1300$ nm with the direct transmission $T = 0.8889$. The nanorods are removed in this simulation, and significant reflection is caused by the planar interface. (d)–(f) Electric field intensity plots with the nanostructure. Each of the resonances decays to three diffraction channels in the dielectric, and in all cases, the field intensity is nearly uniform in air because of excellent antireflection. (d) Steady state electric field intensity at $\lambda = 1236$ nm with transmission $T = 0.9985$. (e) Steady state electric field intensity at $\lambda = 1265$ nm with transmission $T = 0.9975$. (f) Steady state electric field intensity at $\lambda = 1371$ nm with transmission $T = 0.9959$.

to be the background process in Fig. 4(c) ($T = 0.8889$, green dash-dot line), and the coupled-mode theory result (blue dashed curve) is generated using the decay rates from the FDTD simulation of the low-Q resonance at $\lambda = 1236$ nm [Fig. 4(d)]. In the vicinity of this low-Q resonance, the coupled-mode theory and the RCWA simulation agree well. Therefore, we can further regard this low-Q resonance as part of the direct pathway to study light transport at the high-Q resonances. In Fig. 4(b), the green dash-dot curve represents

this direct pathway, which is the numerical spectrum stripped of its resonant features. The coupled-mode theory result (blue dashed curve) in Fig. 4(b) is generated using the decay rates from the FDTD simulations of the two high-Q resonances at $\lambda = 1265$ nm [Fig. 4(e)] and 1371 nm [Fig. 4(f)]. The good agreement with the RCWA simulation result in Fig. 4(b) provides a direct validation of our theory.

The theory above can be applied to antireflection in the practically important air–silicon interface as well. We show that with a relatively low-Q resonance, one can achieve antireflection over a broader bandwidth, and moreover, the effect of antireflection can still be reasonably well described by our theory. We consider a practically significant structure in Fig. 5, where a periodic array of infinitely long cylindrical rods with a radius of 200 nm and a periodicity of 1 μm is placed on an air–substrate interface. Both the nanorods, and the substrate, which is assumed to be infinitely thick in the lower half space, are made of a silicon-like lossless material identical to that used in Fig. 3. Such a structure supports low-Q resonances because the optical resonances supported by the silicon rods have relatively efficient access to the high density of optical states in the high-refractive-index silicon substrate.

In Fig. 6(a), we show the simulated transmission spectrum (red curve) of the structure in Fig. 5. Without the nanostructure, the interface has a transmission of $T = 1 - r^2 = 1 - [(n-1)/(n+1)]^2 = 0.6953$ (green dash-dot line). We plot the steady state electric field intensity in the absence of the nanostructure at $\lambda = 1155$ nm in Fig. 6(b). Again, the interference pattern in air indicates significant reflection at this interface. With the nanostructure, for a sizable bandwidth, the transmission is improved compared to this direct transmission. In particular, at the same wavelength of $\lambda = 1155$ nm, the transmission is unity within numerical accuracy: $T = 0.99999$. The steady state electric field intensity is shown in Fig. 6(c), and reflection is essentially eliminated as the field intensity in air is uniform. In contrast, there is another resonant peak at $\lambda = 1733$ nm with a lower transmission $T = 0.8340$. Figure 6(d) plots its steady state electric field intensity, which shows interference patterns due to significant reflections. To validate the theory, we calculate the theory
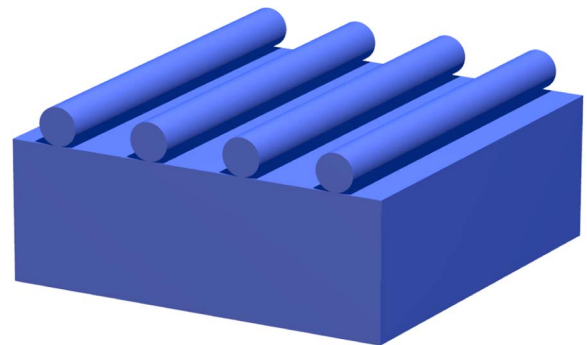

Fig. 5. Low-Q resonant antireflection structure consisting of an array of infinitely long cylindrical rods on an air–dielectric interface. The blue regions represent a silicon-like lossless dielectric with a dielectric constant of 12, and the substrate is assumed to be infinitely thick in the lower half space. The periodicity of the nanorod array is 1 μm. The radius of each rod is 200 nm.
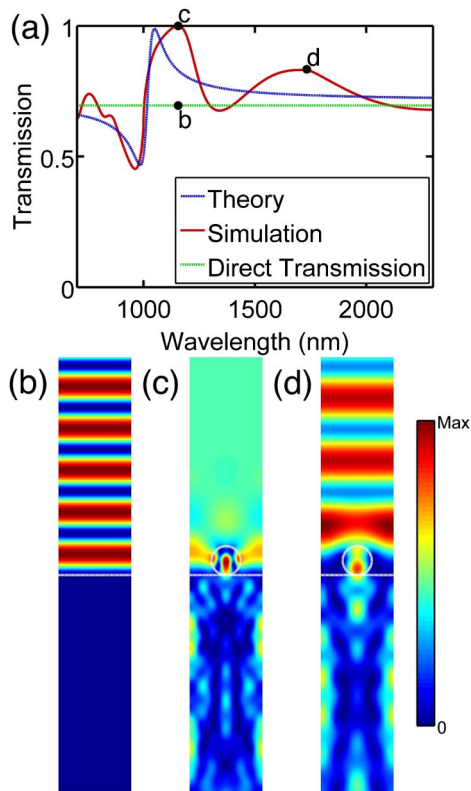
Fig. 6. Transmission spectrum and steady state electric field intensity plots for the structure in Fig. 5 at normal incidence. (a) Comparison of transmission spectra by theory and by simulation. The theory data (blue dashed curve) are computed using Eq. (11) with decay rates obtained from FDTD simulations. The simulation data (red curve) are obtained from RCWA simulation. The direct transmission (green dash-dot line) is determined analytically as $T = 1 - r^2 = 1 - [(n-1)/(n+1)]^2 = 0.6953$, which serves as the background process in Eq. (11). (b)–(d) Electric field intensity plots. The dashed white curves are material boundaries. The colorbar is relative and log-scaled, and red and blue colors correspond to high and low intensities, respectively. (b) Steady state electric field intensity at $\lambda = 1155$ nm with the direct transmission $T = 0.6953$. The nanorods are removed in this simulation, and significant reflection is caused by the planar interface. (c),(d) Electric field intensity plots with the nanostructure. (c) Steady state electric field intensity at $\lambda = 1155$ nm with transmission $T = 0.99999$. The Mie resonance decays to five diffraction channels in the dielectric, and the field intensity is nearly uniform in air because of excellent antireflection. (d) Steady state electric field intensity at $\lambda = 1733$ nm with transmission $T = 0.8340$. The Mie resonance decays to three diffraction channels in the dielectric. Some reflection occurs due to incomplete antireflection.

curve (blue dashed curve) using Eq. (11) for each resonance with $r = (n-1)/(n+1)$. The theory agrees reasonably well with the simulation. In particular, for this system, Eq. (1) is satisfied, and Eq. (12) is approximately satisfied by the decay rates. Therefore, the theory provides adequately accurate guidance for designing broadband resonant antireflection for large refractive index mismatch.

4. DISCUSSION

We have applied the temporal coupled-mode theory to study the resonant antireflection. The formalism developed,

moreover, is general and can be used to study other effects associated with resonant particles at interfaces [58–60]. For example, instead of conditions for antireflection, one can derive conditions for enhanced or perfect reflection [61–65]. Finally, Eq. (1), which represents a sufficient condition for complete antireflection, also represents an optimal condition for light trapping [66,67]. Thus, our theory is useful for understanding the important synergy of simultaneous antireflection and light trapping in these systems [15,28,41].

In comparison with other antireflection schemes, such as the nanocone structure that provides adiabatic impedance transformation [15,18,20,21,68–71], the resonant antireflection scheme tends to have narrower operating wavelength and angular ranges, due to the nature of resonances. Nonetheless, this disadvantage can be mitigated to a certain degree by a number of strategies. For example, in Fig. 4, we note that a single structure can support multiple resonances, all of which may approximately satisfy the condition for perfect antireflection, and in Fig. 6, we show that the resonant linewidth can be increased by placing the resonant structure close to the high-refractive-index dielectric substrate, which possesses high density of optical states. Finally, although the two numerical examples in Section 3 operate in the infrared spectral range, our theory applies to other spectral ranges such as visible frequencies, and the simulated structure can be scaled to operate in the visible wavelength using the same set of material refractive index parameters.

5. CONCLUSION

We have presented a theoretical discussion of the condition of complete antireflection when an array of resonant structures is placed at the air–material interface. To achieve perfect antireflection, the resonant decay in the reflection and transmission directions needs to be balanced, and for normally incident light, the periodicity of the array of nanostructured resonators should be smaller than the wavelength of the incident light in air. The theoretical condition serves as a working guideline for practical resonant antireflection design.

REFERENCES

1. M. Born and E. Wolf, *Principles of Optics*, 7th ed. (Cambridge University, 1999).
2. J. Zhao and M. A. Green, "Optimized antireflection coatings for high-efficiency silicon solar cells," IEEE Trans. Electron Devices **38**, 1925–1934 (1991).
3. M. F. Schubert, F. W. Mont, S. Chhajed, D. J. Poxson, J. K. Kim, and E. F. Schubert, "Design of multilayer antireflection coatings made

from co-sputtered and low-refractive-index materials by genetic algorithm," Opt. Express **16**, 5290–5298 (2008).

4. H. K. Raut, V. A. Ganesh, A. S. Nair, and S. Ramakrishna, "Anti-reflective coatings: a critical, in-depth review," Energ. Environ. Sci. **4**, 3779–3804 (2011).

5. A. Kabiri, E. Girgis, and F. Capasso, "Buried nanoantenna arrays: versatile antireflection coating," Nano Lett. **13**, 6040–6047 (2013).

6. S. P. Huber, R. W. E. van de Kruijs, A. E. Yakshin, E. Zoethout, K.-J. Boller, and F. Bijkerk, "Subwavelength single layer absorption resonance antireflection coatings," Opt. Express **22**, 490–497 (2014).

7. B. S. Thornton, "Limit of the moth's eye principle and other impedance-matching corrugations for solar-absorber design," J. Opt. Soc. Am. **65**, 267–270 (1975).

8. S. J. Wilson and M. C. Hutley, "The optical properties of 'moth eye' antireflection surfaces," J. Mod. Opt. **29**, 993–1009 (1982).

9. W. H. Southwell, "Pyramid-array surface-relief structures producing antireflection index matching on optical surfaces," J. Opt. Soc. Am. A **8**, 549–553 (1991).

10. D. H. Raguin and G. M. Morris, "Antireflection structured surfaces for the infrared spectral region," Appl. Opt. **32**, 1154–1167 (1993).

11. D. G. Stavenga, S. Foletti, G. Palasantzas, and K. Arikawa, "Light on the moth-eye corneal nipple array of butterflies," Proc. R. Soc. B **273**, 661–667 (2006).

12. M. Chen, H.-c. Chang, A. S. P. Chang, S.-Y. Lin, J.-Q. Xi, and E. F. Schubert, "Design of optical path for wide-angle gradient-index antireflection coatings," Appl. Opt. **46**, 6533–6538 (2007).

13. S. S. Oh, C.-G. Choi, and Y.-S. Kim, "Fabrication of mico-lens arrays with moth-eye antireflective nanostructures using thermal imprinting process," Microelectron. Eng. **87**, 2328–2331 (2010).

14. Y. M. Song, S. J. Jang, J. S. Yu, and Y. T. Lee, "Bioinspired parabola subwavelength structures for improved broadband antireflection," Small **6**, 984–987 (2010).

15. K. X. Wang, Z. Yu, V. Liu, Y. Cui, and S. Fan, "Absorption enhancement in ultrathin crystalline silicon solar cells with antireflection and light-trapping nanocone gratings," Nano Lett. **12**, 1616–1619 (2012).

16. S. W. Anzengruber, E. Klann, R. Ramlau, and D. Tonova, "Numerical methods for the design of gradient-index optical coatings," Appl. Opt. **51**, 8277–8295 (2012).

17. J.-Q. Xi, M. F. Schubert, J. K. Kim, E. F. Schubert, M. Chen, S.-Y. Lin, W. Liu, and J. A. Smart, "Optical thin-film materials with low refractive index for broadband elimination of Fresnel reflection," Nat. Photonics **1**, 176–179 (2007).

18. Y.-F. Huang, S. Chattopadhyay, Y.-J. Jen, C.-Y. Peng, T.-A. Liu, Y.-K. Hsu, C.-L. Pan, H.-C. Lo, C.-H. Hsu, Y.-H. Chang, C.-S. Lee, K.-H. Chen, and L.-C. Chen, "Improved broadband and quasi-omnidirectional anti-reflection properties with biomimetic silicon anostructures," Nat. Nanotechnol. **2**, 770–774 (2007).

19. D. J. Poxson, M. F. Schubert, F. W. Mont, E. F. Schubert, and J. K. Kim, "Broadband omnidirectional antireflection coatings optimized by genetic algorithm," Opt. Lett. **34**, 728–730 (2009).

20. S. Chattopadhyay, Y. F. Huang, Y. J. Jen, A. Ganguly, K. H. Chen, and L. C. Chen, "Anti-reflecting and photonic nanostructures," Mater. Sci. Eng. R **69**, 1–35 (2010).

21. A. Deinega, I. Valuev, B. Potapkin, and Y. Lozovik, "Minimizing light reflection from dielectric textured surfaces," J. Opt. Soc. Am. A **28**, 770–777 (2011).

22. P. Spinelli, M. Hebbink, R. de Waele, L. Black, F. Lenzmann, and A. Polman, "Optical impedance matching using coupled plasmonic nanoparticle arrays," Nano Lett. **11**, 1760–1765 (2011).

23. P.-C. Li and E. T. Yu, "Large-area omnidirectional antireflection coating on low-index materials," J. Opt. Soc. Am. B **30**, 2584–2588 (2013).

24. P. Spinelli, M. A. Verschuuren, and A. Polman, "Broadband omnidirectional antireflection coating based on subwavelength surface Mie resonators," Nat. Commun. **3**, 692 (2012).

25. Y. Qiu, H.-C. Hao, J. Zhou, and M. Lu, "A close to unity and all-solar-spectrum absorption by ion-sputtering induced Si nanocone arrays," Opt. Express **20**, 22087–22094 (2012).

26. P. Spinelli, B. Macco, M. A. Verschuuren, W. M. M. Kessels, and A. Polman, "Al2O3/TiO2 nano-pattern antireflection coating with ultra-low surface recombination," Appl. Phys. Lett. **102**, 233902 (2013).

27. M. Beye, A. S. Maiga, and F. Ndiaye, "The effect of the SiN optical constants on the performances of a new antireflection coating concept," in *IEEE Conference on Clean Energy and Technology (CEAT)* (IEEE, 2013), pp. 373–378.

28. A. Lin, Y.-K. Zhong, and S.-M. Fu, "The versatile designs and optimizations for cylindrical TiO2-based scatterers for solar cell anti-reflection coatings," Opt. Express **21**, A1052–A1064 (2013).

29. C. J. Zapata-Rodríguez, J. J. Miret, P. Rodríguez-Cantó, G. M. noz Matutano, J. P. Martínez-Pastor, R. Abargues, D. Pastor, M. Kaiser, and C. Hohle, "Metasurfaces for colour printing," in *16th International Conference on Transparent Optical Networks (ICTON)* (IEEE, 2014), pp. 1–4.

30. L. Chen, X. Jing, L. Wang, J. Zhang, S. Jin, and Y. Tian, "Broadband antireflection enhancement by triangular grating microstructure in the resonance domain," Opt. Laser Technol. **62**, 95–108 (2014).

31. F. Wang, Q.-H. Wei, and H. Htoon, "Generation of steep phase anisotropy with zero-backscattering by arrays of coupled dielectric nano-resonators," Appl. Phys. Lett. **105**, 121112 (2014).

32. T. S. Luk, N. T. Fofang, J. L. Cruz-Campa, I. Frank, and S. Campione, "Surface plasmon polariton enhanced ultrathin nano-structured CdTe solar cell," Opt. Express **22**, A1372–A1379 (2014).

33. I. Kim, D. S. Jeong, W. S. Lee, W. M. Kim, T.-S. Lee, D.-K. Lee, J.-H. Song, J.-K. Kim, and K.-S. Lee, "Silicon nanodisk array design for effective light trapping in ultrathin c-Si," Opt. Express **22**, A1431–A1439 (2014).

34. G. Mie, "Beiträge zur optik trüber medien, speziell kolloidaler metal-lösungen," Ann. Phys. **330**, 377–445 (1908).

35. T. Khudiyev, E. Huseyinoglu, and M. Bayindir, "Nonresonant Mie scattering: emergent optical properties of core-shell polymer nano-wires," Sci. Rep. **4**, 4607 (2014).

36. J. A. Dobrowolski, D. Poitras, P. Ma, H. Vakil, and M. Acree, "Toward perfect antireflection coatings: numerical investigation," Appl. Opt. **41**, 3075–3083 (2002).

37. D. Poitras and J. A. Dobrowolski, "Toward perfect antireflection coatings. 2. Theory," Appl. Opt. **43**, 1286–1295 (2004).

38. A. Szameit, F. Dreisow, M. Heinrich, S. Nolte, and A. A. Sukhorukov, "Realization of reflectionless potentials in photonic lattices," Phys. Rev. Lett. **106**, 193903 (2011).

39. K.-H. Kim and Q.-H. Park, "Perfect anti-reflection from first principles," Sci. Rep. **3**, 1062 (2013).

40. L. V. Thekkekara, V. G. Achanta, and S. D. Gupta, "Optical reflectionless potentials for broadband, omnidirectional antireflection," Opt. Express **22**, 17382–17386 (2014).

41. P. Spinelli and A. Polman, "Light trapping in thin crystalline Si solar cells using surface Mie scatterers," IEEE J. Photovolt. **4**, 554–559 (2014).

42. O. Isabella, J. Kr, and M. Zeman, "Modulated surface textures for enhanced light trapping in thin-film silicon solar cells," Appl. Phys. Lett. **97**, 101106 (2010).

43. J. Zhu, C.-M. Hsu, Z. Yu, S. Fan, and Y. Cui, "Nanodome solar cells with efficient light management and self-cleaning," Nano Lett. **10**, 1979–1984 (2010).

44. Y.-J. Hung, S.-L. Lee, and L. A. Coldren, "Deep and tapered silicon photonic crystals for achieving anti-reflection and enhanced absorption," Opt. Express **18**, 6841–6852 (2010).

45. V. E. Ferry, M. A. Verschuuren, M. C. van Lare, R. E. I. Schropp, H. A. Atwater, and A. Polman, "Optimized spatial correlations for broad-band light trapping nanopatterns in high efficiency ultrathin film a-Si:H solar cells," Nano Lett. **11**, 4239–4245 (2011).

46. J. Grandidier, D. M. Callahan, J. N. Munday, and H. A. Atwater, "Light absorption enhancement in thin-film solar cells using whispering gallery modes in dielectric nanospheres," Adv. Mater. **23**, 1272–1276 (2011).

47. C. Shemelya, D. F. DeMeo, and T. E. Vandervelde, "Two dimensional metallic photonic crystals for light trapping and anti-reflective

coatings in thermophotovoltaic applications," Appl. Phys. Lett. **104**, 021115 (2014).

48. M. K. Hedayati, S. Fahr, C. Etrich, F. Faupel, C. Rockstuhl, and M. Elbahri, "The hybrid concept for realization of an ultra-thin plasmonic metamaterial antireflection coating and plasmonic rainbow," Nanoscale **6**, 6037–6045 (2014).

49. A. Rahman, M. Liu, and C. T. Black, "Block copolymer self assembly for design and vapor-phase synthesis of nanostructured antireflective surfaces," J. Vac. Sci. Technol. B **32**, 06FE02 (2014).

50. S. Fan, W. Suh, and J. D. Joannopoulos, "Temporal coupled-mode theory for the Fano resonance in optical resonators," J. Opt. Soc. Am. A **20**, 569–572 (2003).

51. H. A. Haus, *Waves and Fields in Optoelectronics* (Prentice Hall, 1983).

52. W. Suh, Z. Wang, and S. Fan, "Temporal coupled-mode theory and the presence of non-orthogonal modes in lossless multimode cavities," IEEE J. Quantum Electron. **40**, 1511–1518 (2004).

53. J. D. Joannopoulos, S. G. Johnson, J. N. Winn, and R. D. Meade, *Photonic Crystals: Molding the Flow of Light*, 2nd ed. (Princeton University, 2008).

54. K. X. Wang, Z. Yu, S. Sandhu, and S. Fan, "Fundamental bounds on decay rates in asymmetric single-mode optical resonators," Opt. Lett. **38**, 100–102 (2013).

55. V. Liu and S. Fan, "S^4: a free electromagnetic solver for layered periodic structures," Comput. Phys. Commun. **183**, 2233–2244 (2012).

56. A. Taflove and S. C. Hagness, *Computational Electrodynamics: The Finite-Difference Time-Domain Method*, 3rd ed. (Artech House, 2005).

57. S. Fan and J. D. Joannopoulos, "Analysis of guided resonances in photonic crystal slabs," Phys. Rev. B **65**, 235112 (2002).

58. P. A. Letnes, I. Simonsen, and D. L. Mills, "Substrate influence on the plasmonic response of clusters of spherical nanoparticles," Phys. Rev. B **83**, 075426 (2011).

59. N. S. King, M. W. Knight, N. Large, A. M. Goodman, P. Nordiander, and N. J. Halas, "Orienting nanoantennas in three dimensions to control light scattering across a dielectric interface," Nano Lett. **13**, 5997–6001 (2013).

60. T. E. Karam and L. H. Haber, "Molecular adsorption and resonance coupling at the colloidal gold nanoparticle interface," J. Phys. Chem. C **118**, 642–649 (2014).

61. A. Mizutani, H. Kikuta, K. Iwata, and H. Toyota, "Guided-mode resonant grating filter with an antireflection structured surface," J. Opt. Soc. Am. A **19**, 1346–1351 (2002).

62. H. Butt, Q. Dai, R. Rajasekharan, T. D. Wilkinson, and G. A. J. Amaratunga, "Enhanced reflection from arrays of silicon based inverted nanocones," Appl. Phys. Lett. **99**, 133105 (2011).

63. A. A. Kornyshev, M. Marinescu, J. Paget, and M. Urbakh, "Reflection of light by metal nanoparticles at electrodes," Phys. Chem. Chem. Phys. **14**, 1850–1859 (2012).

64. J. Du, Z. Lin, S. T. Chui, C. Dong, and W. Zhang, "Nearly total omnidirectional reflection by a single layer of nanorods," Phys. Rev. Lett. **110**, 163902 (2013).

65. X.-T. Kong, H. Butt, A. K. Yetisen, C. Kangwanwatana, Y. Montelongo, S. Deng, F. da Cruz Vasconcellos, M. M. Qasim, T. D. Wilkinson, and Q. Dai, "Enhanced reflection from inverse tapered nanocone arrays," Appl. Phys. Lett. **105**, 053108 (2014).

66. Z. Yu, A. Raman, and S. Fan, "Fundamental limit of light trapping in grating structures," Opt. Express **18**, A366–A380 (2010).

67. Z. Yu, A. Raman, and S. Fan, "Fundamental limit of light trapping in solar cells," Proc. Natl. Acad. Sci. USA **107**, 17491–17496 (2010).

68. S. Wang, B. D. Weil, Y. Li, K. X. Wang, E. Garnett, S. Fan, and Y. Cui, "Large-area free-standing ultrathin single-crystal silicon as processable materials," Nano Lett. **13**, 4393–4398 (2013).

69. K. X. Wang, Z. Yu, V. Liu, M. L. Brongersma, T. F. Jaramillo, and S. Fan, "Nearly total solar absorption in ultrathin nanostructured iron oxide for efficient photoelectrochemical water splitting," ACS Photonics **1**, 235–240 (2014).

70. K. X. Wang, J. R. Piper, and S. Fan, "Optical impedance transformer for transparent conducting electrodes," Nano Lett. **14**, 2755–2758 (2014).

71. L. Zhu, A. Raman, K. X. Wang, M. A. Anoma, and S. Fan, "Radiative cooling of solar cells," Optica **1**, 32–38 (2014).